A p-adaptive high-order mesh-free framework for fluid simulations in complex geometries

Ruofeng Feng[*] and Jack R. C. King[†]

Department of Mechanical and Aerospace Engineering, University of Manchester, UK

Steven J. Lind

School of Engineering, Cardiff University, Cardiff, UK

(Dated: November 27, 2025)

This paper presents a novel p-adaptive, high-order mesh-free framework for the accurate and efficient simulation of fluid flows in complex geometries. High-order differential operators are constructed locally for arbitrary node distributions using linear combinations of anisotropic basis functions, formulated to ensure the exact reproduction of polynomial fields up to the specified p order. A dynamic p-refinement strategy is developed to refine (increase) or de-refine (decrease) the polynomial order used to approximate derivatives at each node. A new refinement indicator for mesh-free methods is proposed, based on local error estimates of the Laplacian operator, and is incorporated into the solution procedure at minimal added computational cost. Based on this error indicator, a refinement criterion is established to locally adjust the polynomial order p for the solution. The proposed adaptive mesh-free scheme is then applied to a range of canonical PDEs, and its potential is demonstrated in two-dimensional simulations of a compressible reacting flow in porous media. For the test cases studied, the proposed method exhibits potential to save up to 50% of computational costs while maintaining the specified level of accuracy. The results confirm that the developed p-adaptive high-order mesh-free method effectively captures highly non-linear regions where high-order approximation is necessary and reduces computational costs compared to the non-adaptive method, preserving high accuracy and solution stability.

Keywords: High-order; Mesh-free; Error-based indicator; p-adaptivity; Fluid simulation; Porous media

I. INTRODUCTION

Simulating fluid problems via the numerical solution of partial differential equations (PDEs) relies on the accurate calculation of spatial derivatives from field values at a discrete set of points. High-order approximations are particularly desirable, as they can achieve extremely high accuracy with lower resolution, thereby reducing computational costs. High-order finite difference (FD)[1] and spectral methods[2], for instance, are easily constructed on structured meshes but they are consequently limited to simple geometries. While immersed boundary methods can extend these approaches to complex geometries, they face significant challenges in accurately imposing boundary conditions[3]. Conversely, methods such as unstructured finite volume (FV)[4] and finite element methods address the challenge of handling complex geometries. Their primary difficulty, however, is that accuracy is highly dependent on mesh quality. In such cases, generating a high-quality, body-fitted unstructured mesh with minimal skewed elements becomes a major bottleneck. This process can be so resource-intensive, in some cases, such as porous media, taking longer than the simulation itself, that it undermines the efficiency of the method[5].

Mesh-free methods offer an alternative to traditional grid-based approaches by operating on a set of computational points (often called particles) without requiring information on topological connectivity. A key advantage of mesh-free methods is that discretizing a complex geometry with an unstructured set of nodes is straightforward and easily automated (e.g.,[6]). Many of these methods, particularly strong-form variants, work by constructing differential operators on a local stencil of collocation points. They have several variants, including radial basis function (RBF) methods [7–12], generalized finite difference methods (GFDM)[13–15], generalized moving least squares (GMLS) methods [16, 17], reproducing kernel particle methods (RKPM) [18, 19], and finite particle methods (FPM) [20–23]. The specific order of approximation can be constructed using various basis functions (e.g., orthogonal polynomials, Taylor monomials) and techniques (e.g., weighted or moving least squares). A primary challenge for these collocation-based methods is ensuring the conservation of physical quantities (such as mass and momentum), a difficulty inherent to the strong-form formulation. In this regard, Smoothed Particle Hydrodynamics (SPH) stands out as a popular alternative that inherently preserves preserves mass (and momentum depending on the formulation) ([24]) and has

---

been applied to a wide range of applications ([25–30]). However, a major limitation of SPH is its accuracy, in which traditional Lagrangian SPH is often restricted to low-order convergence rates as resolution increases. In recent years, high-order formulations of SPH have been widely explored to improve the consistency, such as consistency corrections to kernels [31] and derivative operators [32], Riemann-type formulations[33, 34], W/TENO reconstruction[35], and a hybrid spectral scheme[36]. The Local Anisotropic Basis Function Method (LABFM), proposed by King et al.[37], is another variant of high-order mesh-free methods. It constructs derivative operators from a weighted sum of local field value differences, where the weights are formed from a linear combination of Anisotropic Basis Functions (ABFs) to guarantee polynomial consistency of a specified order. LABFM may be formulated at higher orders (commonly up to 10th order) and has a lower computational cost for a given level of accuracy compared to other consistent mesh-free methods[38]. Nevertheless, for the practical application of high-order mesh-free methods, the major obstacle remains their intensive computational cost due to large stencils to achieve higher-order consistency.

Adaptive solution strategies are an important approach for balancing computational efficiency and high accuracy. These techniques are particularly effective for problems where high resolutions are required only in localized regions, such as simulating the dynamic evolution of fine flame fronts. Two primary adaptive approaches have been proposed in the literature: p-adaptivity, and h-adaptivity. In p-adaptivity, the accuracy is varied by locally adjusting the order of the interpolant approximation. In contrast, h-adaptivity locally adjusts the resolution of the spatial discretization. h-adaptivity has seen widespread adoption in mesh-based methods for fluid dynamics, commonly known as adaptive mesh refinement (AMR) techniques. Notable examples include Basilisk[39], which utilizes a quadtree/octree-based grid structure with a second-order accurate FV discretization, the AMReX library[40], which employs a block-structured approach to manage nested patches of successively finer grids, and the HAMISH code[41], which combines adaptive Cartesian grids with a high-order scheme using fourth-order flux reconstruction methods. p-adaptivity, on the other hand, has been frequently explored within high-order numerical frameworks such as spectral element methods (SEM)[42, 43] and discontinuous Galerkin (DG) methods[44, 45] to improve the convergence rate. hp-adaptivity is another adaptive strategy, e.g.,[46, 47], that integrates h- and p- refinement. With the incorporation of the hp-decision strategy often based on the measure of solution smoothness, the method allocates p-refinement to regions with a smooth solution, while h-refinement is applied to non-smooth regions.

In the context of mesh-free methods, h-adaptivity can be implemented by adding or removing computational nodes [48], without the issues associated with mesh-based methods (e.g., topological data update [49], hanging nodes[50], and mesh quality[51]). h-adaptivity has been studied extensively for various mesh-free methods, such as GFDM[52], RBF-FD[53], GMLS[54], and SPH[55]. While considerable research has been contributed to h-adaptive mesh-free methods, few studies have been devoted to p-adaptivity. The very recent study by Jančič and Kosec [56] has achieved p-refinement in RBF-FD for the linear elasticity problem. However, due to the need of explicit re-evaluations of the PDEs at a higher order approximation for the refinement indicator, the adaptive solution may become more expensive than the non-adaptive method.

In light of these challenges, this work presents a p-adaptive high-order mesh-free scheme built upon LABFM. A novel refinement indicator is proposed, which is derived from a local estimate of the error associated with the mesh-free approximation of second-order differential operators. This indicator is then used to establish a procedure that locally adapts the polynomial order, p, according to user-defined error thresholds, with low additional computational costs. The performance and accuracy of the proposed p-adaptive LABFM are evaluated on a range of benchmark tests, including a standard test function convergence study, the viscous Burgers' equation, and the Kelvin-Helmholtz instability. Finally, the proposed method is applied to simulate compressible reacting flows, investigating the propagation of hydrogen–air flames in both unconfined and confined geometries. The computational speed-up achieved through p-adaptivity is discussed. To the best of the authors' knowledge, this is the first time that p-adaptivity has been enabled within a mesh-free framework for fluid simulations.

The remaining part of this paper is organised as follows: Section II presents a brief description of the LABFM methodology for high-order spatial discretisation. In Section III, the formulation of the refinement indicator as well as the p-adaptivity strategy is introduced. The accuracy and performance of the developed method are examined in Section IV through a number of numerical benchmark tests. Finally, conclusions are summarised in Section V.

II. HIGH-ORDER MESH-FREE SCHEME

The high-order mesh-free scheme adopted in this study follows the Local Anisotropic Basis Function Method (LABFM) [37]. LABFM has demonstrated up to 10th-order convergence, even for node distributions with significant local disorder [38]. This allows the method to remain extremely accurate, even in complex geometries where non-uniformity in the node distribution is unavoidable.

A.   Evaluation of spatial derivatives

To start with, we define a general expression for the spatial derivative as follows,

$$L^d(\cdot) = \mathbf{C}^d \cdot \mathbf{D}(\cdot) \tag{1}$$

where d is the index that identifies the partial derivative under consideration, $\mathbf{D}(\cdot)$ is the vector of partial derivatives that is expressed as,

$$\mathbf{D}(\cdot) = \left[\frac{\partial(\cdot)}{\partial x}, \ \frac{\partial(\cdot)}{\partial y}, \ \frac{\partial^2(\cdot)}{\partial x^2}, \ \frac{\partial^2(\cdot)}{\partial x \partial y}, \ \frac{\partial^2(\cdot)}{\partial y^2}, \ \frac{\partial^3(\cdot)}{\partial x^3}, \ \frac{\partial^3(\cdot)}{\partial x^2 \partial y}, \ \frac{\partial^3(\cdot)}{\partial x \partial y^2}, \ \frac{\partial^3(\cdot)}{\partial y^3}, \ \frac{\partial^4(\cdot)}{\partial x^4}, \cdots \right]^T \tag{2}$$

in which $\mathbf{C}^d$ is a vector pointing to the derivatives for a given index d. For example, to estimate the gradients and Laplacian of a function, for which case $L^x = \partial/\partial x$, $L^y = \partial/\partial y$, $L^L = \nabla^2$, $\mathbf{C}^d$ can be expressed as,

$$\mathbf{C}^d = \begin{cases} \left[1, 0, 0, 0, 0, 0, \ldots\right]^T & \text{if } d = x \\ \left[0, 1, 0, 0, 0, 0, \ldots\right]^T & \text{if } d = y \\ \left[0, 0, 1, 0, 1, 0, \ldots\right]^T & \text{if } d = L \end{cases} \tag{3}$$

The mesh-free construction of spatial derivatives in Eq. (1) to a specified p order of consistency follows the methodology of LABFM. In the following, only the essential components of LABFM are presented. For a detailed description of the methodology, readers are referred to [37, 57].
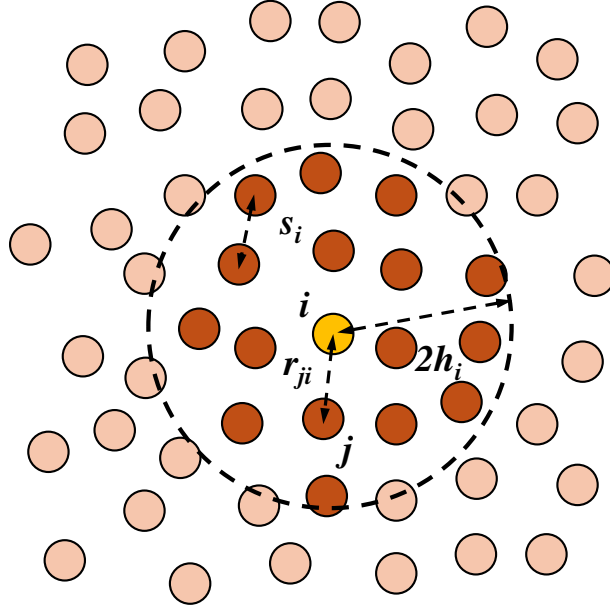

FIG. 1. An illustration of the computational stencil.

In LABFM, the computational domain is discretized as a set of N unstructured nodes, as illustrated in Fig. 1. Each node $i \in [1, N]$ has position vector $\boldsymbol{r}_i = (x_i, y_i)^T$, a distribution length scale s_i, and a characteristic stencil length scale h_i. The distribution length scale s_i represents the local average inter-node distance and serves as a resolution metric. The resolution may vary spatially, allowing for non-uniform spatial adaptivity. The computational stencil for node i contains $\mathcal{N}_i$ neighboring nodes j satisfying $|\boldsymbol{r}_{ji}| \leq 2h_i$. The neighbour count for 2D problem approximately follows $\mathcal{N}_i \approx 4\pi(h_i/s_i)^2$, with the ratio h_i/s_i characterizing stencil size. Property differences between nodes are defined as $(\cdot)_{ji} = (\cdot)_j - (\cdot)_i$.

The general discrete operator at a computational node i to reproduce the spatial derivative in Eq. (1) is given by,

$$L^d(\cdot)_{i,h,p} = \sum_j (\cdot)_{ji} w_{ji}^d \tag{4}$$

where the subscript h and p represent the local stencil length scale and local polynomial order adopted in the interpolation, respectively. w_{ji}^d are the set of weights. Here (and throughout), the summation over j is over all $\mathcal{N}_i$ nodes within the stencil of node i.

In Eq. (4), the weights w_{ji}^d in LABFM are constructed as the weighted sum of a series of Anisotropic Basis Functions (ABFs) $\mathbf{W}_{ji} = \mathbf{W}(r_{ji}/h_i)$, given by

$$w_{ji}^d = \mathbf{W}_{ji} \cdot \mathbf{\Psi}^d{}_i \tag{5}$$

Following [38] the ABFs are constructed from bi-variate Hermite polynomials multiplied by a radial basis function (RBF) ψ, with the α-th component of $\mathbf{W}_{ji}$ expressed as,

$$W_{ji}^\alpha = \frac{\psi(r_{ji}/h_i)}{\sqrt{2^{\alpha_1+\alpha_2}}} \, H_{\alpha_1}\left(\frac{x_{ji}}{h_i\sqrt{2}}\right) H_{\alpha_2}\left(\frac{y_{ji}}{h_i\sqrt{2}}\right), \tag{6}$$

where H_a is the a-th order univariate Hermite polynomial, the radial basis function ψ adopted in this work is the Wendland C2 kernel [58], α_1 and α_2 are the x and y exponents of the α-th bi-variate Taylor monomial.

To ensure the general discrete operator in Eq. (4) has polynomial consistency of order p, the weighting vector $\mathbf{\Psi}^d$ is evaluated by solving a linear system given by,

$$\mathbf{M}_i \cdot \mathbf{\Psi}^d{}_i = \mathbf{C}^d \tag{7}$$

where $\mathbf{M}_i$ is the moment matrix at node i for recovering the p-th order consistency, calculated as,

$$\mathbf{M}_i = \sum_j \mathbf{X}_{ji} \otimes \mathbf{W}_{ji}, \tag{8}$$

in which $\mathbf{X}_{ji}$ is the vector of monomials,

$$\mathbf{X}_{ji} = \left[x_{ji}, \ y_{ji}, \ \frac{x_{ji}^2}{2}, \ x_{ji}y_{ji}, \ \frac{y_{ji}^2}{2}, \frac{x_{ji}^3}{6}, \ \frac{x_{ji}^2 y_{ji}}{2}, \ \frac{x_{ji}y_{ji}^2}{2}, \ \frac{y_{ji}^3}{6}, \frac{x_{ji}^4}{24}, \ \dots \ \frac{y_{ji}^p}{p!} \right]^T, \tag{9}$$

To ensure polynomial consistency of order p, we include the first $n = (p^2 + 3p)/2$ terms in Eq. (9). As a result, the leading order of error becomes $\mathcal{O}(s_i^{p+1-l})$, where l is the order of the derivative being approximated. For example, the LABFM approximation of the first-order derivative converges with s^p, while the second-order derivative with s^{p-1}.

III. p-ADAPTIVITY PROCEDURES

A. Local refinement indicator

A crucial component of any adaptive strategy is the refinement indicator, the criterion used to decide where the resolution/order should be refined or de-refined. The refinement indicators can be broadly classified into three categories: feature-based, error-based, and goal-oriented[44]. Feature-based indicators[59], which identify the key physical features that need to be fully resolved, are computationally cheap and easy to implement, making them highly effective for capturing sharp features like shockwaves; however, their main drawback is that they are not a true measure of numerical error and can fail to refine regions where the error is large but the solution is smooth. In contrast, error-based indicators are more mathematically rigorous, evaluating the error in numerical solutions based residuals or recovery-based methods[60, 61]. They offer the advantage of providing a more reliable and general approximation of the actual discretization error, but at the cost of increased computational expenses. The primary advantage of goal-oriented (adjoint-based) indicators [62] is their efficiency in optimizing the resolution for a specific quantity of interest (e.g., aerodynamic lift); their disadvantage, however, is their high memory requirements and high computational cost for the solution of the adjoint problem[44].

In this study, we utilize the concept of discretisation error-based indicators to provide direct control over the numerical accuracy of the solution. Inspired by the small-scale energy density indicator [44, 63] and the spectral decay indicator [64], which involves projecting the solution onto a reduced-order space for error estimation and has proven effectiveness in p-adaptive mesh-based simulations of fluid problems [44] , this work formulates the indicator in a similar manner. However, in strong-form high-order mesh-free methods, the local construction of lower-order solutions requires substantial additional computational cost, which diminishes the benefits of adaptivity.

To enable a low-cost adaptive procedure, the proposed indicator is formulated using the Laplacian operator, which can be readily incorporated into the existing derivative evaluations within the numerical solver. This type of refinement

indicator can also effectively reflect the solution error, since the discretization error of the Laplacian operator is essential for the solution of PDEs in fluid problems . The refinement indicator η_i at node i is defined as,

$$\eta_i = \left| L^L(\phi)_{i,h,p} - L^L(\phi)_{i,h,p-\delta p} \right| \tag{10}$$

where ϕ is the field variable under consideration. δp is the variation of the polynomial order in the refinement. In this work, the polynomial order operates in the range of even orders (e.g., $p = 2, 4, 6, 8...$) for a monotonic change of error magnitude and $\delta p = 2$ is applied for all the analysis. $L^L(\phi)_{i,h,p-\delta p}$ is the Laplacian of ϕ on the reduced-order space.

B. Refinement criteria

The following refinement criteria are adopted for the refinement or de-refinement of the polynomial order p_i used for LABFM approximation at a given node i , after the estimation of the local refinement indicators η_i.

$$p_i = \begin{cases} p_i + \delta p & \text{if } \eta_i > \varepsilon_U \ \& \ p_i < p_{\max} \\ p_i - \delta p & \text{if } \eta_i < \varepsilon_L \ \& \ p_i > p_{\min} \\ p_i & \text{otherwise} \end{cases} \tag{11}$$

where ε_U and ε_L are the user-defined limits of the indicator ($\varepsilon_U > \varepsilon_L$). Their values depend on the specific requirement of error level and typically range between $[10^{-8}, 10^{-1}]$. p_{max} and p_{min} are respectively the maximum and minimum polynomial order. In this study, p_{max} is set as 8, while the p_{min} is set as 4.

Since the approximation with a reduced polynomial order employs a smaller stencil compared to that of the original polynomial order, the refinement indicator can be evaluated within the same loop used for the existing Laplacian approximation, incurring only a minor increase in computational cost. The polynomial order distribution generated at the current time step is used as the initial condition for the subsequent time step. As flow features are advected, the refinement indicator may yield large values, prompting an increase in the local polynomial order to accurately capture these features. By assigning lower polynomial orders with smaller stencils in regions of lesser complexity, the overall computational cost is reduced while maintaining the error within a user-defined threshold.

It is noted that Eq. (10) may be rewritten as,

$$\eta_i = \left| [L^L(\phi)_{i,h,p} - \nabla^2(\phi)_i] - [L^L(\phi)_{i,h,p-\delta p} - \nabla^2(\phi)_i] \right| \tag{12}$$

which is equivalent to,

$$\eta_i = \left| \varepsilon_{h,p}^L - \varepsilon_{h,p-\delta p}^L \right| \tag{13}$$

Clearly, the refinement indicator measures the error difference in the Laplacian approximation between the original polynomial order and the reduced polynomial order. In addition, since in most cases, the term $\varepsilon_{h,p-\delta p}^L$ in Eq. (13) is the dominant term, the refinement indicator approximates the error of the solution on the reduced-order space and the refinement criteria control the error magnitude of the projection of the solution onto the reduced-order space. This will be discussed in the following section IV.

IV. NUMERICAL TESTS

In this section, the p-adaptive LABFM is applied to a range of test cases. First, the convergence behaviour of the proposed method is examined to assess how the approximation error is controlled by the thresholds employed in the refinement criteria. Next, the accuracy and performance of the p-adaptive method are demonstrated using the travelling wave solution and the periodic solution of the viscous Burgers' equation, as well as the Kelvin–Helmholtz instability. Finally, the proposed method is applied to the simulation of compressible reacting flows in complex geometries, where it is validated against free-propagating hydrogen flames, before being applied to the simulation of flame propagation in porous materials.

A. Convergence test

This test case evaluates the fundamental error behaviour of gradient and Laplacian approximations using the p-adaptive LABFM, over a range of resolutions. A sinusoidal function and a super-Gaussian function are chosen as test functions. The sinusoidal profile is smooth with uniformly distributed errors, making it ideal for analysis of the performance of refinement indicators with varying error thresholds. In contrast, the super-Gaussian features a localized jump with steep gradients, providing a benchmark for testing the adaptive algorithm.

In this case, a unit square domain defined by $(x, y) \in [0, 1] \times [0, 1]$ is considered. The tested sinusoidal function is given by

$$\phi(x, y) = \sin(k\pi \hat{x}) \sin(k\pi \hat{y}) \tag{14}$$

where $\hat{x} = x - 0.1453$, $\hat{y} = y - 0.16401$, and k is the wave number, set as $k = 2$ in this case. Note that a pseudo-random offset is introduced into the function to add asymmetry. This prevents the cancellation of numerical errors that might otherwise occur when analyzing symmetric function profiles.

For p order equal to 4, 6, and 8, the stencil size ratio h/s is taken as 2.3, 1.8, and 1.4, respectively. Nodes are initially distributed on a uniform Cartesian grid with resolution s and then subjected to random perturbations. Following [37], the maximum perturbation distance is set as ϵ and the resulting perturbation magnitude ϵ/s is taken as a measure of distribution irregularity, in which $\epsilon/s = 0.5$ is applied in this study. To ensure full stencil support near boundaries, ghost nodes are generated within a boundary strip of width $2h$, following the same resolution and distribution irregularity as interior nodes. The field properties at the boundary nodes are prescribed with their analytical values. The p-adaptive LABFM method is validated by computing approximations of the gradient and Laplacian of ϕ across multiple resolutions. The initial polynomial order is set to $p = 6$, while local adjustments of p order are governed by the adaptive algorithm according to the defined error threshold. Errors are quantified using the normalized L_2-norm. Due to the nearly uniform error distribution in approximating the sinusoidal function, we expect the local error control would be reflected in the global error behaviour.
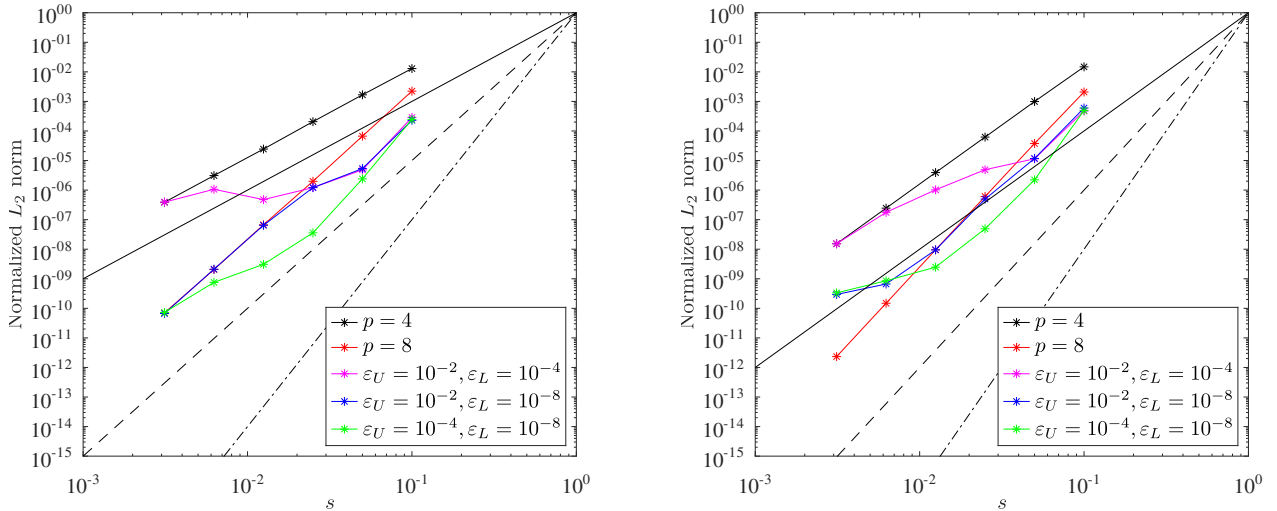

FIG. 2. Convergence behaviour of the differential operator approximation using the adaptive and non-adaptive methods, showing Laplacian approximation (left) and gradient approximation (right).

Three sets of threshold are tested, including $\varepsilon_U = 10^{-2}$, $\varepsilon_L = 10^{-4}$; $\varepsilon_U = 10^{-2}$, $\varepsilon_L = 10^{-8}$; and $\varepsilon_U = 10^{-4}$, $\varepsilon_L = 10^{-8}$. The convergence behaviour of the Laplacian and gradient approximation of the sinusoidal function, as s halved successively from $1/10$ to $1/320$, is shown in Fig. 2. As discussed in section III B, the error indicator reflects the error magnitude in the reduced order space. Therefore, in this case, as the resolution varies, a refinement or de-refinement of p order occurs when the error at that resolution projected to the lower-order space reaches a threshold. For example, this is indicated in the Laplacian approximation by the shift from the convergence rate of $p = 6$ to $p = 4$ as resolution increases in the line representing $\varepsilon_U = 10^{-2}$, $\varepsilon_L = 10^{-4}$ and the shift from the convergence rate of $p = 6$ to $p = 8$ as resolution decreases in the line representing $\varepsilon_U = 10^{-4}$, $\varepsilon_L = 10^{-8}$, both of which occur at a resolution of $s = 1/40$. In the former case, the error reaches lower threshold $\varepsilon_L = 10^{-4}$ while in the latter it hits the upper

threshold $\varepsilon_U = 10^{-4}$. When the error exceeds the upper threshold ε_U, the interpolation switches to a higher p order for a greater convergence rate. Conversely, if the error is below the lower threshold ε_L, the interpolation with a lower p order is activated. In between the upper and lower threshold, the original p order remains (or, globally, a mix of different p orders for non-uniformly distributed errors). This implies that the algorithm will allocate more computation resources to regions identified as having high error, defined by the upper threshold, while less computational focus will be placed on regions with low error, defined by the low threshold, enabling efficient computation according to the predefined accuracy level. It is found that the refinement procedure can also effectively adjust the error behaviour of gradient approximation according to the given thresholds. While the change in convergence rate is observed to occur earlier for the gradient approximation than for the Laplacian approximation as the spatial resolution increases, this is reasonable because the error from the gradient approximation is often smaller than that of the Laplacian, with a convergence rate typically one order of magnitude higher.

In the following test, the super Gaussian function is adopted, given by,

$$\phi(x, y) = \exp\left[-32\pi^4(\hat{x}^4 + \hat{y}^4)\right] \tag{15}$$

where the same pseudo-random offset is introduced for $\hat{x}$ and $\hat{y}$ as in the sinusoidal test function, i.e., equation (14).

Fig. 3 shows the relationships between the error and the cost by $p = 8$ and p-adaptivity $[\varepsilon_U = 10^{-5}, \varepsilon_L = 10^{-8}]$, as well as the local polynomial order when using the adaptive method. Herein, the cost is quantified by a measure, the average neighbour count divided by the resolution $\langle \mathcal{N} \rangle / s^2$, which is proportional to the computational cost. As shown in Fig. 3, it is clear that the adaptive algorithm effectively captures regions with steep gradients that require high-order polynomial reconstruction. For the same computational cost, the p-adaptive algorithm achieves higher accuracy than a fixed polynomial order. For example, for $\langle \mathcal{N} \rangle / s^2 = 10^6$, the Laplacian approximation with $p = 8$ leads to the normalized L_2 norm error of the order of 10^{-5}, while the p-adaptivity results in an error of the order of 10^{-6}.
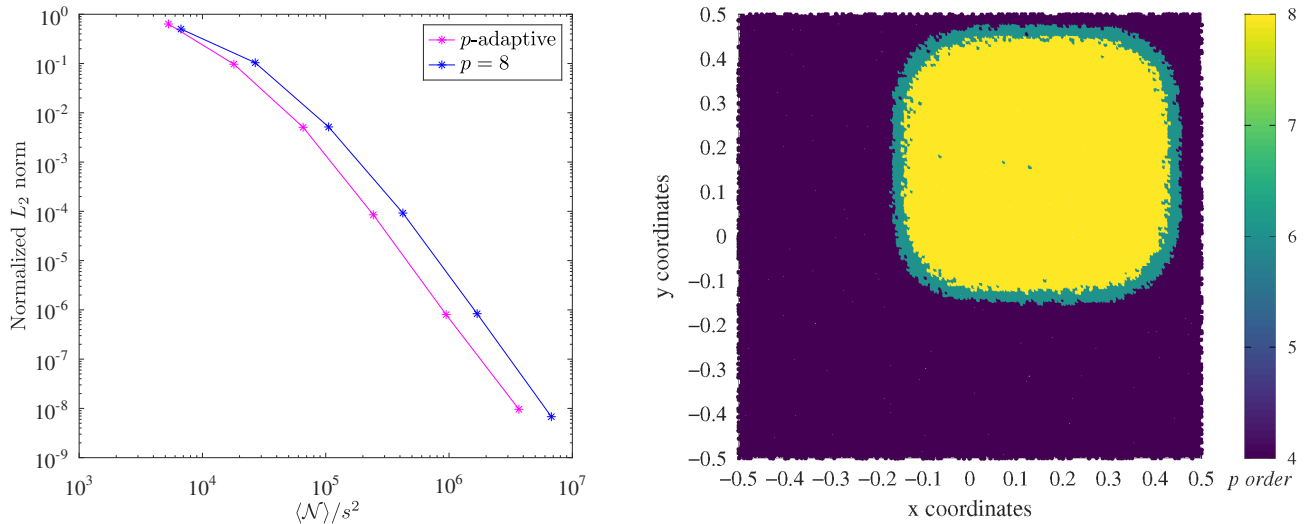

FIG. 3. Convergence test results using the adaptive method, showing error versus cost with comparison against the non-adaptive method (left) and local polynomial order p (right).

B. Viscous Burgers' equation

In this case, the p-adaptive LABFM is tested on solving the viscous Burgers' equation, which is a mixed hyperbolic-parabolic PDE featured by the development of shock. The viscous Burgers' equation is written as,

$$\frac{\partial \mathbf{u}}{\partial t} + \mathbf{u} \cdot \nabla \mathbf{u} = \frac{1}{Re} \nabla^2 \mathbf{u} \tag{16}$$

where Re is the Reynolds number. We use LABFM (adaptive or non-adaptive) to evaluate spatial derivatives, and an explicit fourth order Runge-Kutta (RK4) scheme for time integration. The adopted time step (dimensionless) for

the solution of Eq. (16) is given by,

$$\delta t = \min\left(\frac{0.2h}{\max\|\mathbf{u}\|}, 0.05h^2 Re\right) \tag{17}$$

1. Travelling wave test case

The first test involves a traveling wave moving diagonally along the xy-plane, where the steepening caused by non-linear advection is balanced by viscous diffusion. As the Reynolds number increases, the wave becomes steeper. The computational domain is a unit-square defined by $(x, y) \in [0, 1] \times [0, 1]$ and discretized using a perturbed Cartesian node distribution with $\epsilon/s = 0.2$. To ensure complete stencil support at boundaries, the node distributions near boundary are extended outward, and the analytical solutions are imposed on these exterior nodes. The initial conditions and analytic solution are given by:

$$u(x, y, t) = \frac{3}{4} - \frac{1}{4\left(1 + e^{Re(-t-4x+4y)/32}\right)}, \tag{18}$$

$$v(x, y, t) = \frac{3}{4} + \frac{1}{4\left(1 + e^{Re(-t-4x+4y)/32}\right)}. \tag{19}$$

We vary the (spatially uniform) resolution from $s = 1/10$ to $s = 1/160$. The initial polynomial order is taken as $p = 8$. The Reynolds number Re is taken as 200 and 500 for two distinct wave profiles. The upper and lower threshold are set as $\varepsilon_U = 10^{-3}$ and $\varepsilon_L = 10^{-6}$.
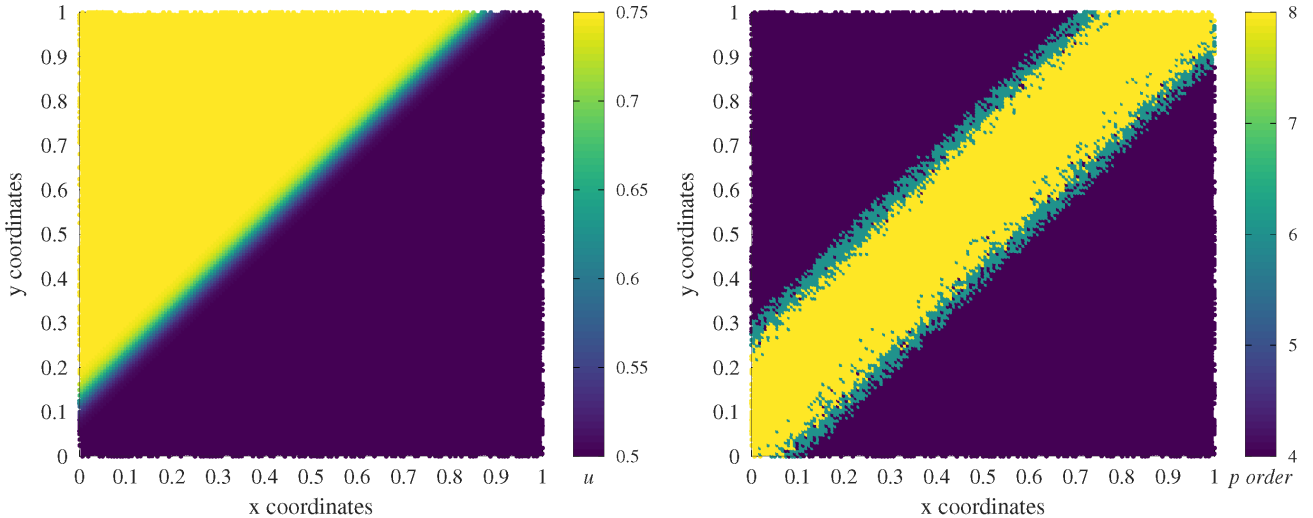

FIG. 4. Numerical solution of the travelling wave case using the adaptive method [$Re = 500$, $s = 1/160$, $t = 0.5$], showing the value of u (left) and local polynomial order p (right).

Fig. 4 and Fig. 5 show the numerical solution of u and the local polynomial order for the simulation with $Re = 200$ and $Re = 500$, respectively, with a node spacing of $s = 1/160$ at $t = 0.5$. The adaptive algorithm is shown to capture the moving wave profile and effectively locate the region with nonlinearity. It is also noted that the case with $Re = 200$ exhibits a narrower range of the highest polynomial order and a wider range of medium polynomial order compared to the case with $Re = 500$. This is expected because the wave profile for $Re = 200$ is smoother than that for $Re = 500$, and the spatial distribution of error remains flatter for $Re = 200$. The convergence of error for this case is shown in Fig. 6. The convergence behaviour of the error by p-adaptivity for both $Re = 200$ and $Re = 500$, across the given resolutions from $s = 1/10$ to $s = 1/160$, is similar to that with a fixed polynomial order of $p = 8$. However, the p-adaptive method exhibits a clear reduction in computational cost, as shown in the right panel of Fig. 6. This reduction is more pronounced at higher Reynolds numbers, where the wave profile becomes steeper and narrower. For the node spacing of $s = 1/160$, the adaptive algorithm can improve the accuracy by one order of magnitude

compared to the non-adaptive method at the same $\langle\mathcal{N}\rangle/s^2$. No cost reduction is observed at the first few coarsest node resolutions. This is attributed to the local error being greater than the upper threshold $\varepsilon_U = 10^{-3}$, resulting in the highest p-order activated across the entire domain without any local adaptation.
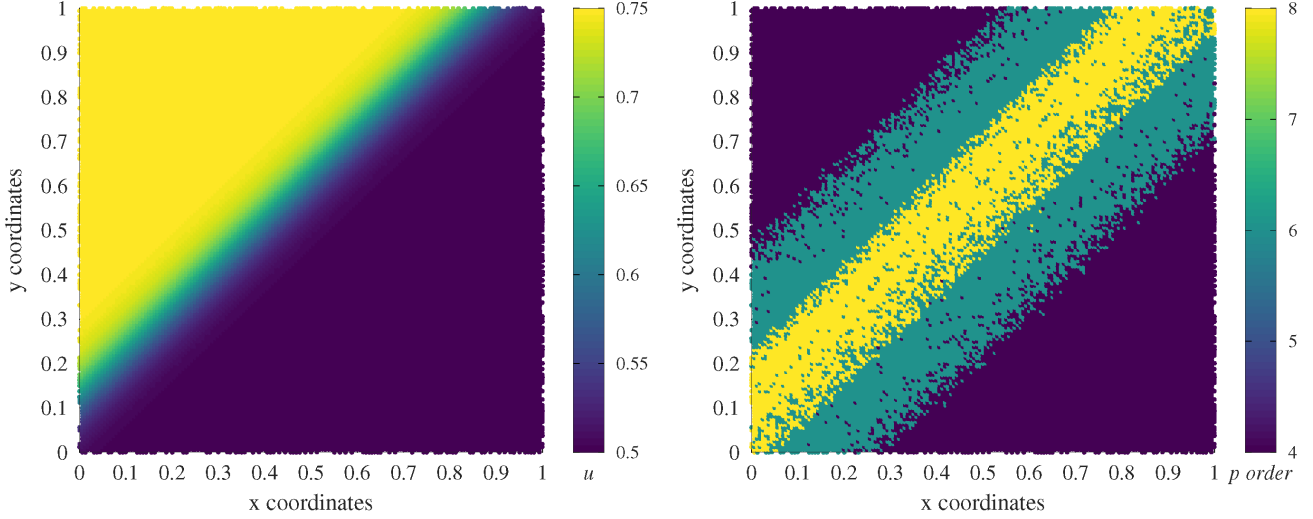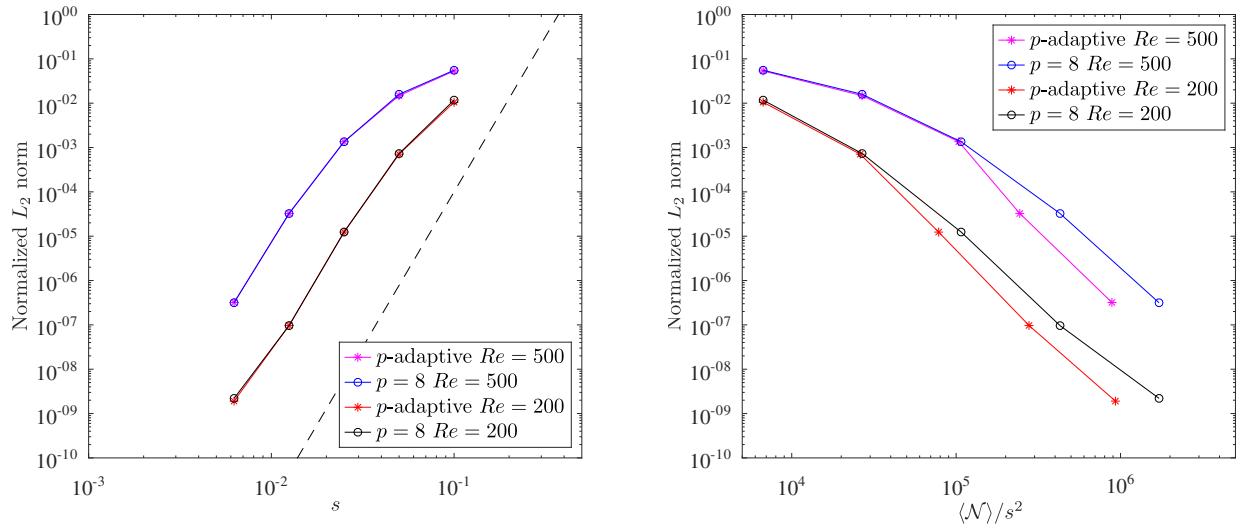

FIG. 5. Numerical solution of the travelling wave case using the adaptive method [$Re = 200$, $s = 1/160$, $t = 0.5$], showing the value of u (left) and local polynomial order p (right).

FIG. 6. Error analysis of the traveling wave test at $t = 1$ for $Re = 200$ and $Re = 500$, using the p-adaptive method and the non-adaptive method with $p = 8$. The left panel shows the convergence behaviour of the error, while the right panel shows the error versus computational cost at $s = 1/160$.

2. Periodic test case

The second case refers to the solution of the viscous Burgers' equation on a unit periodic square domain. The initial velocity condition is defined by a sinusoidal function given by $u(x, y, 0) = \sin(2\pi x)$ and $v(x, y, t) = 0$. The analytic solution, derived via the Cole-Hopf transformation was first given in [65]. Three initial node spacings $s = 1/40$,

$s = 1/80$, and $s = 1/160$ are tested on an unstructured node distribution with the relative perturbation amplitude of $\epsilon/s = 0.2$. The Reynolds number Re is taken as 100. The refinement thresholds match those of the traveling wave case, with $\varepsilon_U = 10^{-3}$ for refinement and $\varepsilon_L = 10^{-6}$ for coarsening.

In Fig. 7, the comparisons of numerical solution against the analytical solution at different time instants are presented, together with the plot of local polynomial order at $t = 0.5$. The initial sinusoidal profile gradually develops into a shock due to the contribution of the advection term and then dissipates under the effect of the viscous term. The p-adaptive LABFM matches well with the analytical solution. The proposed p-adaptive algorithm effectively captures the shock region while allowing lower polynomial orders elsewhere, resulting in a stable, accurate, and efficient solution.
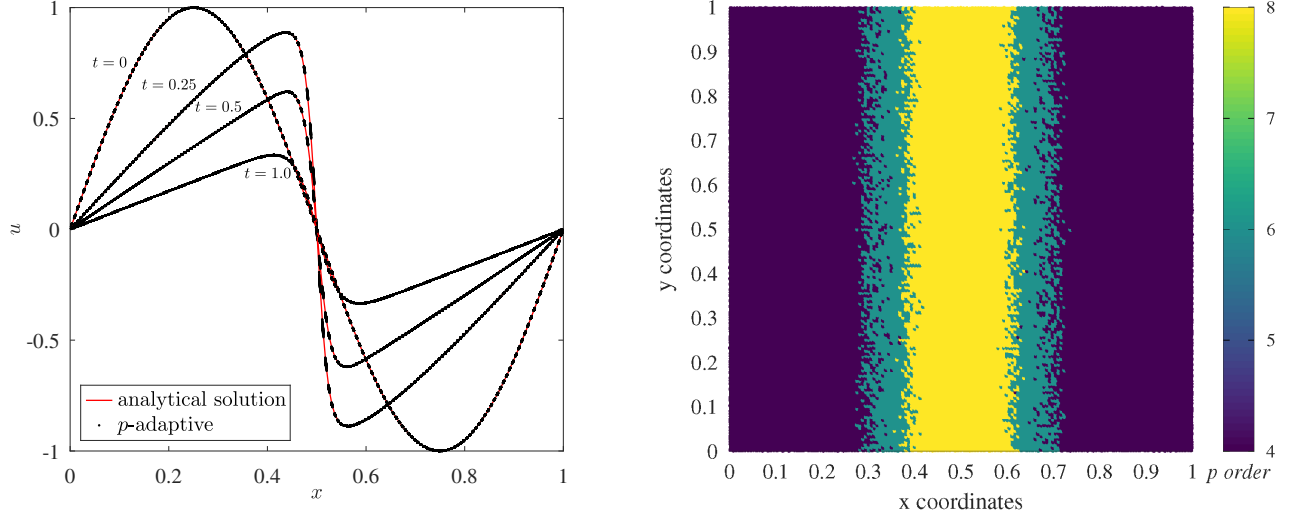

FIG. 7. Numerical solution of the periodic viscous Burger's equations, showing the time evolution of u against analytical solution (left) and local polynomial order p (right) [$Re = 100$, $s = 1/160$, $t = 0.5$].
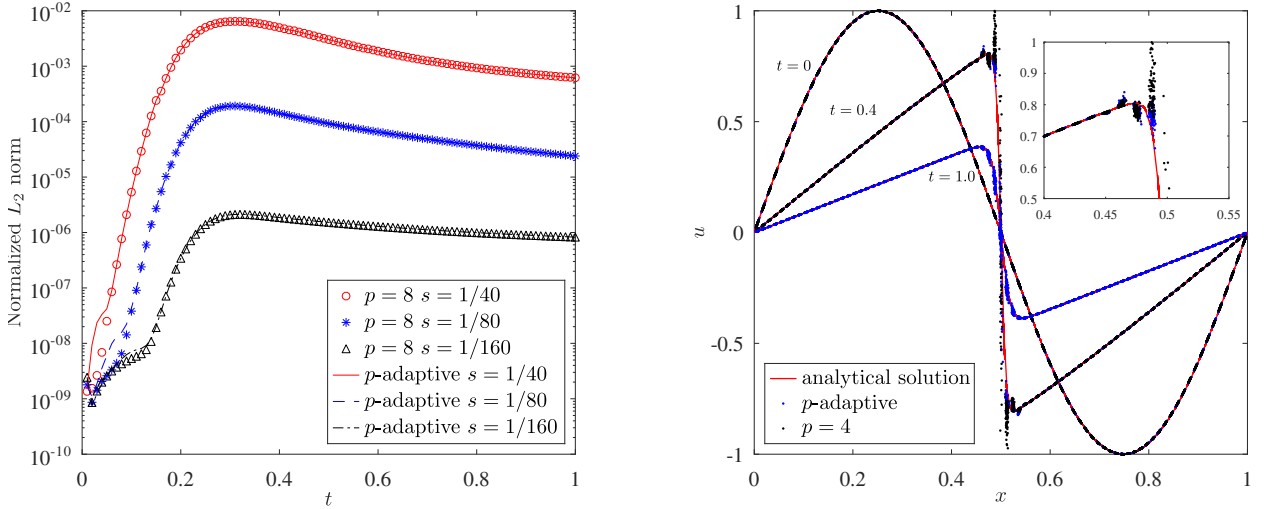

FIG. 8. Time evolution of the error in the periodic viscous Burger's test by the p-adaptive method and the non-adaptive method with $p = 8$ at resolutions of $s = 1/40$, $s = 1/80$, and $s = 1/160$, using $\epsilon/s = 0.2$ and $Re = 100$ (left) and time evolution of u against the analytical solution, with the numerical solution obtained by the p-adaptive method (blue dots) and the non-adaptive method with $p = 4$ (black dots) at resolutions of $s = 1/80$, using $\epsilon/s = 0.4$ and $Re = 250$ (right).

The variation of L_2-norm error with time for the resolutions of $s = 1/40$, $s = 1/80$, and $s = 1/160$ is shown in Fig. 8. Errors increase during the initial advection-dominated phase as the sinusoidal profile steepens and subsequently decrease during the viscosity-dominated phase. Except for the initial few time instances, where the error is very low and reaches the threshold for coarsening, the error from the p-adaptivity is nearly identical to that from a fixed polynomial order of 8.

A further investigation is conducted with a configuration where the Reynolds number is increased to $Re = 250$ and the disorder in the node distribution is increased to $\epsilon/s = 0.4$. As shown in the right panel of Fig. 8, the results using a uniform $p = 4$ exhibit overshoots around the shock, which eventually lead to numerical instability and failure of the simulation (no results after around $t = 0.5$). This occurs because the shock profile is under-resolved when using low polynomial orders, causing the solution to become unstable and necessitating higher-order approximations in these regions [37]. By contrast, the proposed adaptive algorithm, which varies the p order from 4 to 8, effectively identifies the shock region and mitigates the instability, leading to an accurate and stable simulation.

C. Kelvin–Helmholtz instability

Next we study the Kelvin–Helmholtz instability, a fluid instability that occurs at the interface between two fluids due to shear [66–68]. In this case, an initial sinusoidal perturbation was given to the two-fluid system at the interface. The node distribution without perturbations is used for comparable simulations, as randomly distributed node positions can alter the instability pattern from case to case.

The dimensionless two-phase Navier-Stokes equations for this case are expressed as

$$\frac{\partial \rho}{\partial t} + \boldsymbol{u} \cdot \nabla \rho = -\rho \nabla \cdot \boldsymbol{u}$$
$$\frac{\partial \boldsymbol{u}}{\partial t} + \boldsymbol{u} \cdot \nabla \boldsymbol{u} = -\nabla p_f + \frac{1}{Re} \nabla^2 \boldsymbol{u}$$
$$\frac{\partial Y}{\partial t} + \boldsymbol{u} \cdot \nabla Y = \frac{1}{Re\,Sc} \nabla^2 Y$$

where p_f is the fluid pressure, Re is the Reynolds number, Fr is the Froude number, Sc denotes the Schmidt number, and At represents the Atwood number.

The governing equations are closed by Barotropic equation of state for two fluids, given by,

$$p_f = \frac{1}{Ma^2} \left(\rho - Y - (1 - Y) \frac{1 - At}{1 + At} \right) \tag{20}$$

The initial conditions are set as follows:

$$u = 1/2, \quad v = 0, \quad Y = 0, \quad \rho = (1 - At)/(1 + At) \quad \forall \quad y \in [0.5 + \delta \sin(2\pi x), 1]$$
$$u = -1/2, \quad v = 0, \quad Y = 1, \quad \rho = 1 \quad \forall \quad y \in [0, 0.5 + \delta \sin(2\pi x)]$$

where is δ the disturbance coefficient for creating the instability, which is taken as 0.05 in this work.

The time steps (dimensionless) for numerical solution are constrained by the speed of sound, advection and diffusion, given by,

$$\delta t = \min \left\{ \frac{0.1h}{u_{\max} \left(1 + \frac{1}{Ma} \right)}, \ 0.05h^2 Re \min(1, Sc) \right\} \tag{21}$$

The flow properties for the two-phase flow are set as $Re = 500$, $Sc = 8$, $Ma = 0.1$, and $At = 0.2$. The node resolution is set as $s/H = 160$. The upper and lower threshold are taken as $\varepsilon_U = 10^{-1}$ and $\varepsilon_L = 10^{-4}$.

Figures 9 and 10 show the evolution of the volume fraction at $t = 1$ and $t = 2$, respectively, along with their corresponding local polynomial orders. The interpolated interface of the two-phase flow (defined as the location where $Y = 0.5$) is also plotted. The growth and roll-up of perturbations into the formation of typical cat-eye structures in the Kelvin–Helmholtz instability [69, 70] is reproduced using the p-adaptive LABFM and the evolution of local polynomial orders marches with the changing vortex structures.

Fig. 11 presents the calculated time evolution of the total kinetic energy (KE), normalized by the initial kinetic energy (KE_0), using a fixed polynomial order ($p = 8$) and p-adaptivity. It is found that, although part of the domain adapts to a lower polynomial order through the adaptive algorithm, the calculated KE remains the same as the results obtained using the highest polynomial order.
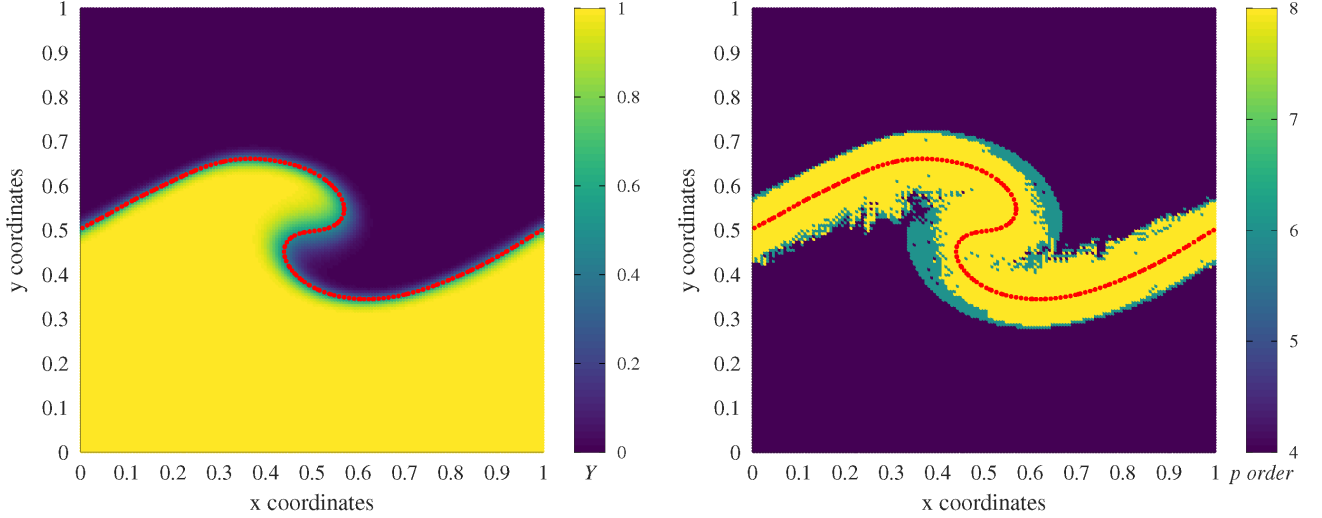
FIG. 9. The numerical solution of the Kelvin–Helmholtz instability at $t = 1$ using the adaptive method, showing the volume fraction evolution (left) and local polynomial order p (right), where the red line represents the interpolated interface.
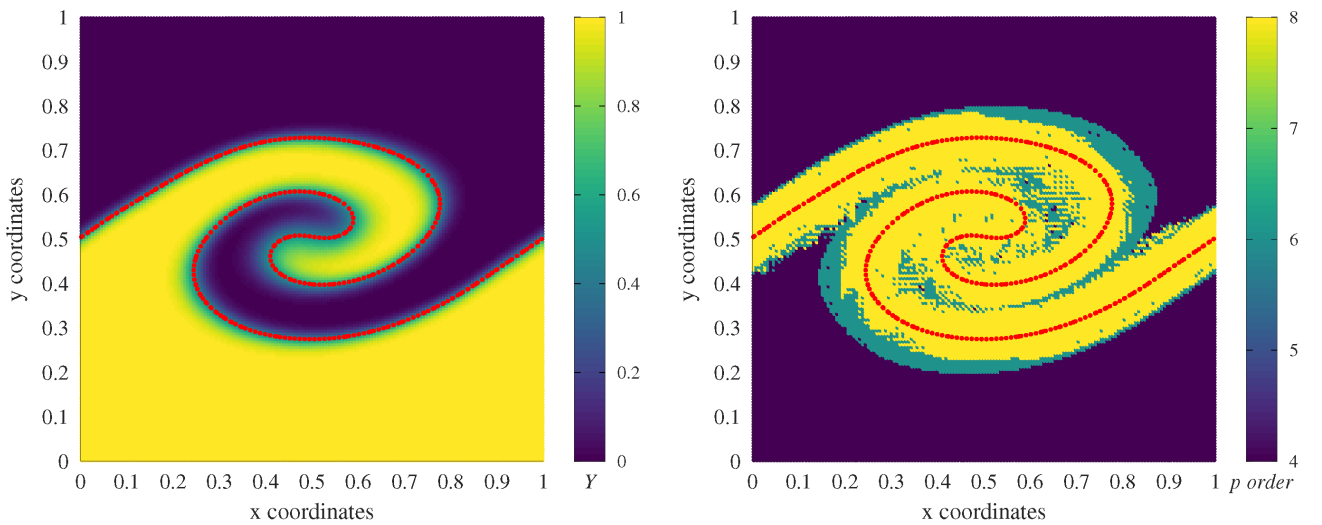

FIG. 10. The numerical solution of the Kelvin–Helmholtz instability at $t = 2$ using the adaptive method, showing the volume fraction evolution (left), and local polynomial order p (right), where the red line represents the interpolated interface.

D. Compressible reacting flows

The proposed method is finally applied to the simulation of compressible reacting flows. The compressible Navier-Stokes equations for a mixture of N_S miscible reacting chemical species are solved with the p-adaptive LABFM. The governing equations, written in index notation with Greek subscripts denoting spatial coordinates and Latin subscripts indicating physical entities such as phases or species for clarity, are given by,
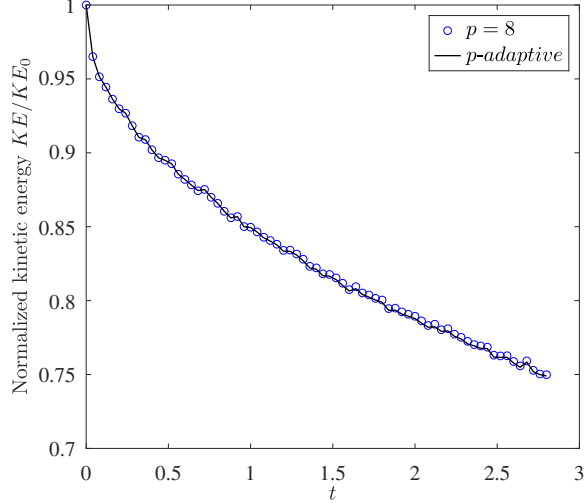
FIG. 11. Time evolution of the normalised kinetic energy KE/KE_0 over time for the non-adaptive method $p = 8$ and the adaptive method

$$\frac{\partial \rho}{\partial t} + \frac{\partial \rho u_\alpha}{\partial x_\alpha} = 0 \tag{22}$$

$$\frac{\partial \rho u_\alpha}{\partial t} + \frac{\partial \rho u_\alpha u_\beta}{\partial x_\beta} = -\frac{\partial p_f}{\partial x_\alpha} + \frac{\partial \tau_{\alpha\beta}}{\partial x_\beta} + \rho f_\alpha \tag{23}$$

$$\frac{\partial \rho E}{\partial t} + \frac{\partial \rho u_\alpha E}{\partial x_\alpha} = -\frac{\partial p_f u_\alpha}{\partial x_\alpha} - \frac{\partial q_\alpha}{\partial x_\alpha} + \frac{\partial \tau_{\alpha\beta} u_\alpha}{\partial x_\beta} + \rho \sum_{k=1}^{N_S} Y_k f_\alpha (u_\alpha - V_{\alpha.k}) \tag{24}$$

$$\frac{\partial \rho Y_k}{\partial t} + \frac{\partial \rho u_\alpha Y_k}{\partial x_\alpha} = \dot{\omega}_k - \frac{\partial \rho V_{\alpha.k} Y_k}{\partial x_\alpha}, \quad \forall k \in [1, N_S] \tag{25}$$

where u_α is the velocity component in the α-direction, $\tau_{\alpha\beta}$ is the component of viscous stress tensor, f_α is the body force, q_α is the heat flux vector, Y_k is the mass fraction of species $k \in [1, N_S]$, $V_{\alpha.k}$ is the molecular diffusion velocity of species k in the α-direction, and $\dot{\omega}_k$ is the production rate of species k. The total energy E has a relationship with other thermodynamic quantities via the caloric equation of state according to,

$$E = \sum_k h_k Y_k - \frac{p_f}{\rho} + \frac{1}{2} u_\alpha u_\alpha \tag{26}$$

where h_k is the enthalpy of species k.

The governing equations are closed by the thermal equation of state

$$p_f = \rho R_0 T \sum_k Y_k / W_k \tag{27}$$

where R_0 is the universal gas constant, T is the temperature, W_k is the molar mass of species k.

The temperature dependencies of thermodynamic quantities (i.e., heat capacity $c_{p,k}$, enthalpy h_k) for each species follow polynomial forms fitted to standard NASA polynomials [71]. Two reaction mechanisms are utilized in this work for hydrogen flames, including the 21-step, 9-species hydrogen-air mechanism of [72], and a single-step irreversible Arrhenius mechanism as in [73]. The latter is constructed for dilute hydrogen combustion and is tuned to match the laminar flame speed of hydrogen at atmospheric pressure and an equivalence ratio, i.e., the actual ratio of fuel-to-oxidizer in a mixture to the stoichiometric ratio, of 0.32. For this mechanism, the temperature dependence of transport properties is prescribed via a power law with an exponent of 0.7, and a constant Lewis number approximation is applied for molecular diffusion, allowing the thermal conductivity and molecular diffusivities to be determined from the definitions of the Prandtl and Lewis numbers. For the multi-step reaction mechanism, a mixture-averaged model for

transport properties is employed, following the combination rules of [74, 75], with the Hirschfelder-Curtiss approximation for molecular diffusion [76]. Soret and Dufour effects are neglected, consistent with [77]. Time integration is performed using an explicit third-order Runge-Kutta scheme. The implementation of p-adaptive LABFM for compressible reacting flow simulation, as described above, is achieved within the message passing interface (MPI)-enabled DNS combustion code, the SUNSET code (**S**calable **U**nstructured **N**ode-**SET** code) [78]. A detailed description of the mathematical model and numerical implementation is available in [57].

1. Freely-propagating H_2-air flames

This case simulates planar, laminar, freely propagating stoichiometric hydrogen-air flames. A rectangular two-dimensional domain is considered, with length $L_x = L = 10mm$ and a narrow aspect ratio, $L_y = L/40$. The domain is periodic in y, with inflow and outflow boundaries in x. The temperature at the inflow is set to $T_{in} = 300K$, the velocity to $U = 2.05m/s$, and mass fractions corresponding to a stoichiometric hydrogen-air mixture are imposed. A partially non-reflecting outflow condition [57] is used to maintain an outflow pressure of $p_{f.out} = 10^5 Pa$. The 9-species, 21-step reaction mechanism of [72] is employed.
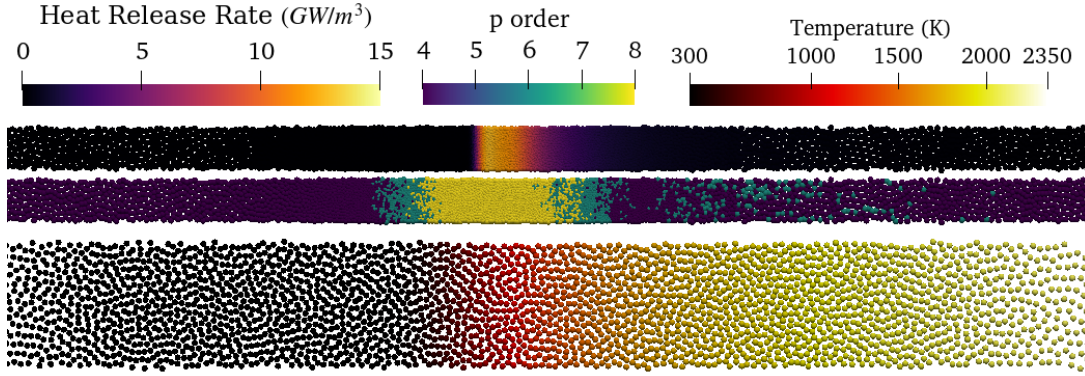

FIG. 12. Results and node distribution for the planar laminar hydrogen-air flame simulations: heat release rate (top), p order (middle), and temperature (bottom)
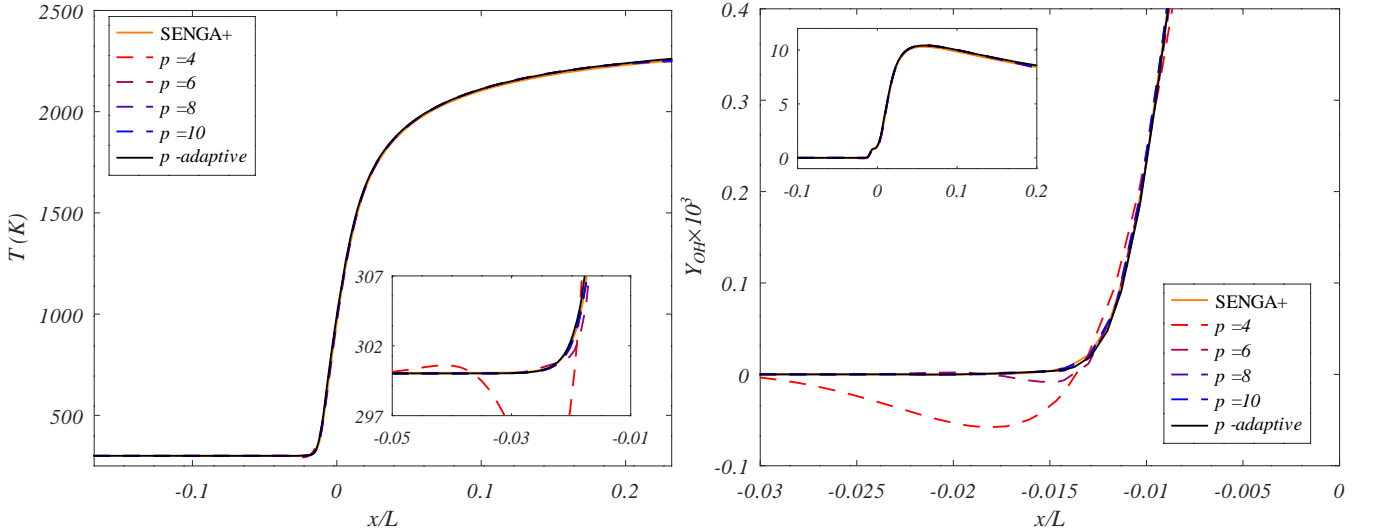

FIG. 13. Spatial profiles of temperature (left) and OH mass fraction (right) for a freely propagating stoichiometric hydrogen-air flame, obtained with the present adaptive code (black lines), with the non-adaptive version at order $m \in [4, 6, 8, 10]$ (dashed lines), and SENGA+ (orange line). In all cases, the resolution is $L/1000$.

For the discretization, $s/L = 0.003$ is set at the inflow and outflow boundaries, reduced linearly over a region of $0.1L$ to $s/L = 0.001$ in the central $0.1L$ of the domain, corresponding to a resolution of $s = 10\mu m$. This configuration

ensures that the flame structure is resolved by at least 10 nodes. The upper and lower threshold for adaptivity are taken as $\varepsilon_U = 10^{-3}$ and $\varepsilon_L = 10^{-4}$. The simulation is run until a steady flame profile is achieved.

Figure 13 shows the spatial profiles of temperature (left) and the hydroxide OH mass fraction (right) for a freely propagating hydrogen-air flame, obtained using the present adaptive method, the non-adaptive version at orders $p \in [4, 6, 8, 10]$, and the reference code SENGA+ [79]. SENGA+ is one of the leading codes for combustion DNS based on a tenth-order finite difference scheme with a fourth-order explicit Runge–Kutta method for time integration. Localized differences are observed for $p = 4$ and 6 compared to other results. A possible reason could be the lower resolving power for smaller p order, resulting in insufficient resolution to accurately compute the advection terms. This leads to slight oscillatory behaviour just upstream of the flame front, with local minima in temperature and regions of unphysical negative OH mass fraction. For $p \geq 8$, these oscillations are absent, and the results closely match the reference solution. Notably, the p-adaptive scheme, which varies the order p from 4 to 8, eliminates the issues associated with uniformly low-order schemes while achieving accuracy comparable to the uniform $p = 8$ case. In addition, the p-adaptive code achieves a speed-up of approximately 15–20% compared to the uniform $p = 8$ case. Note that the current implementation is based on an MPI-enabled parallel scheme with static domain decomposition, indicating promising potential for further increase of computational speed-up with the implementation of dynamic load balancing.

2. Flame propagation through a cylinder array

In this case, the adaptive scheme is applied to the analysis of a hydrogen flame propagating through a porous matrix constructed from an array of cylinders. This scenario features complex geometries and dynamic flame front evolution. The propagation of the flame is investigated within an idealized porous medium represented by a hexagonal array of cylinders.
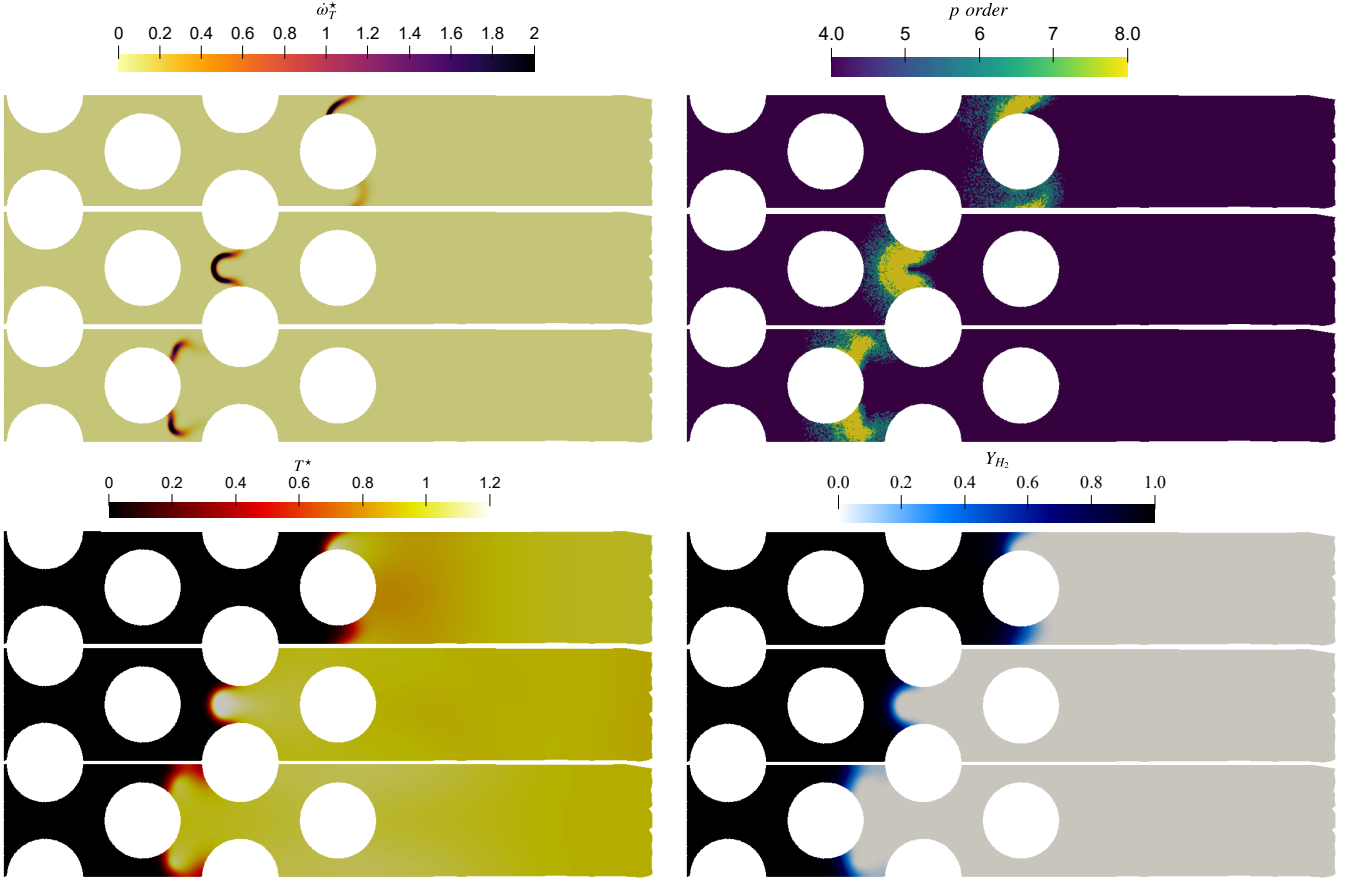

FIG. 14. Time evolution of a hydrogen flame propagating through a porous matrix at $t^* = 11$ (first row), $t^* = 18$ (second row), and $t^* = 23$ (thrid row), showing the heat release rate $\dot{\omega}_T^*$ (top left), the local polynomial order p (top right), the temperature T^* (bottom left), and the mass fraction Y_{H_2} (bottom right).

The hydrogen-air mixture under consideration has an equivalence ratio of $\phi = 0.32$, at atmospheric pressure and a temperature of $300K$. The laminar flame speed and thermal flame thickness are $S_L \approx 0.07m/s$ and $\delta_L \approx 1mm$, respectively, serving as reference scales for non-dimensionalization. The cylinder diameter is fixed at $D/\delta_L = 5$, while the cylinder spacing is taken as $S/D = 5/3$. The computational domain consists of a rectangular region with a length of $10D$ and a width of S. Lateral boundaries are periodic, while streamwise boundaries employ non-reflecting inflow and outflow conditions, as described in [57]. The temperature at the inflow is set to $T_{in} = 300K$, while the outflow boundary tracks a pressure of $p_{f,out} = 10^5 Pa$. Adiabatic no-slip conditions are imposed on the cylinder surfaces. The domain is discretised with a non-uniform resolution, varying from $s_{min} = D/80$ at the cylinder surface, to $s_{out} = 6s_{min}$ at the outflow, and $s_{in} = s_{min}$ at the inflow. As in the previous test, the upper and lower thresholds for adaptivity are set as $\varepsilon_U = 10^{-3}$ and $\varepsilon_L = 10^{-4}$. The simulations are initialized with a laminar flame positioned just downstream of the cylinder array and perturbed by a small, random, multi-mode disturbance with an amplitude of $\delta_L/4$.

Fig. 14 shows the contour plot of the heat release rate, the temperature, the mass fraction of H_2, and the local polynomial order during the flame propagation through pore structures at different time instants. The flame propagates relatively evenly through each pore, with a uniform evolution of Y_{H_2}. An enhanced heat release rate is observed as the flame passes through the pore throat, alongside a local increase of temperature. The dynamic evolution of the p order aligns well with the flame's propagation. This demonstrates that the adaptive algorithm effectively captures the flame front, a region where high-order accuracy is necessary, as it propagates through a complex geometry.
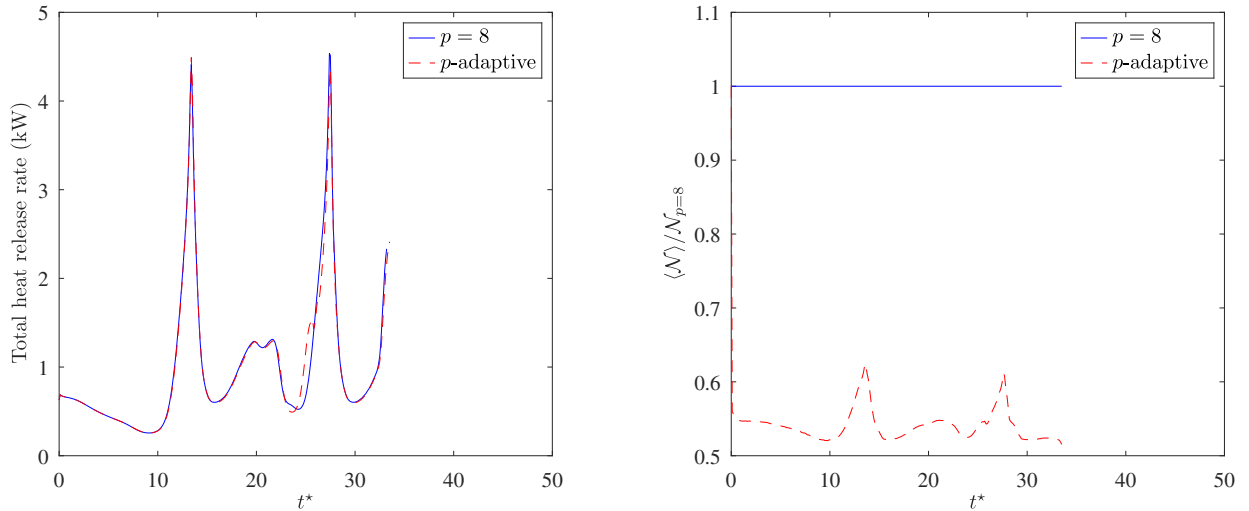

FIG. 15. Comparison of results obtained using p-adaptivity and non-adaptivity with $p = 8$, showing time evolution of the integrated heat release rate (left) and the normalized neighbouring count (right).

The time evolution of the integrated heat release rate and the normalized neighbour counts per node, comparing fixed $p = 8$ and p-adaptivity, is shown in Fig. 15. The heat release fluctuates as the flame propagates through the pores, while the adaptive algorithm captures the varied heat release and adjusts accordingly. The results for the heat release rate obtained using the p-adaptive method are nearly identical to those obtained with $p = 8$, although a small discrepancy occurs at around $t^* = 23$. This could be attributed to the thermal diffusivity being sensitive to discretization error. However, the computational cost for mesh-free interpolation, represented by the neighbour counts per node, is reduced by nearly half with the adaptive algorithm. This demonstrates the improved computational efficiency and high accuracy possible with the proposed p-adaptive mesh-free approach.

V. CONCLUSIONS

In this work, a p-adaptive, high-order mesh-free scheme based on the Local Anisotropic Basis Function Method (LABFM) is developed for flow problems in complex geometries. A refinement indicator based on the mesh-free estimate of local discretisation error of the Laplacian operator is formulated, and a corresponding refinement strategy is investigated to increase/decrease the order of the LABFM polynomial reconstruction at local computational nodes.

The performance of the new p-adaptive mesh-free scheme is tested through several benchmark tests and compared with the original LABFM with a uniform polynomial order. The results demonstrate that the developed p-adaptive LABFM effectively captures regions where high accuracy is necessary and adjusts the approximation order accordingly. This approach leads to improved solution stability compared to a fixed low-order method, while achieving comparable accuracy to a fixed high-order method with better computational efficiency. The new mesh-free p-adaptive algorithm is then applied to resolve flame-structure interactions in complex geometries, showing a notable reduction in computational cost compared to the non-adpative high-order implementation while maintaining high accuracy.

However, it is also worth mentioning that when extending the proposed method to parallel computation, there could be an issue of unbalanced load distribution due to the adaptive algorithm. In such a situation, a dynamic domain partition or task-based parallelism may be needed to realise the potential speedup. A parallel p-adaptive LABFM with a dynamic load-balancing technique will be a subject of future investigation.

ACKNOWLEDGMENTS

[1] S. K. Lele, Compact finite difference schemes with spectral-like resolution, Journal of Computational Physics **103**, 16 (1992).

[2] G. E. Karniadakis, Spectral element simulations of laminar and turbulent flows in complex geometries, Applied numerical mathematics **6**, 85 (1989).

[3] A. H. Rauch, A. Konduri, J. Chen, H. Kolla, and H. K. Chelliah, DNS investigation of cavity stabilized premixed turbulent ethylene-air flame, in *2018 AIAA Aerospace Sciences Meeting* (2018) p. 1674.

[4] H. G. Weller, G. Tabor, H. Jasak, and C. Fureby, A tensorial approach to computational continuum mechanics using object-oriented techniques, Computers in physics **12**, 620 (1998).

[5] B. D. Wood, X. He, and S. V. Apte, Modeling turbulent flows in porous media, Annual Review of Fluid Mechanics **52**, 171 (2020).

[6] B. Fornberg and N. Flyer, Fast generation of 2-D node distributions for mesh-free PDE discretizations, Computers & Mathematics with Applications **69**, 531 (2015).

[7] E. Kansa, Multiquadrics - A scattered data approximation scheme with applications to computational fluid-dynamics - I surface approximations and partial derivative estimates, Computers & Mathematics with Applications **19**, 127 (1990).

[8] E. Kansa, Multiquadrics - A scattered data approximation scheme with applications to computational fluid-dynamics - II solutions to parabolic, hyperbolic and elliptic partial differential equations, Computers & Mathematics with Applications **19**, 147 (1990).

[9] C. Shu, H. Ding, and K. Yeo, Local radial basis function-based differential quadrature method and its application to solve two-dimensional incompressible Navier-Stokes equations, Computer Methods in Applied Mechanics and Engineering **192**, 941 (2003).

[10] T. Cecil, J. Qian, and S. Osher, Numerical methods for high dimensional Hamilton-Jacobi equations using radial basis functions, Journal of Computational Physics **196**, 327 (2004).

[11] G. B. Wright, *Radial Basis Function Interpolation: Numerical and Analytical Developments*, Ph.D. thesis, Boulder, CO, USA (2003), aAI3087597.

[12] B. Fornberg and N. Flyer, Solving PDEs with radial basis functions, Acta Numerica **24**, 215–258 (2015).

[13] P. S. Jensen, Finite difference techniques for variable grids, Computers & Structures **2**, 17 (1972).

[14] J. Benito, F. Ureña, and L. Gavete, Solving parabolic and hyperbolic equations by the generalized finite difference method, Journal of Computational and Applied Mathematics **209**, 208 (2007).

[15] L. Gavete, F. Ureña, J. Benito, A. García, M. Ureña, and E. Salete, Solving second order non-linear elliptic partial differential equations using generalized finite difference method, Journal of Computational and Applied Mathematics **318**, 378 (2017).

[16] N. Trask, M. Perego, and P. Bochev, A High-Order Staggered Meshless Method for Elliptic Problems, SIAM Journal on Scientific Computing **39**, A479 (2017).

[17] N. Trask, M. Maxey, and X. Hu, A compatible high-order meshless method for the Stokes equations with applications to suspension flows, Journal of Computational Physics **355**, 310 (2018).

[18] W. K. Liu, S. Jun, S. Li, J. Adee, and T. Belytschko, Reproducing kernel particle methods for structural dynamics, International Journal for Numerical Methods in Engineering **38**, 1655 (1995).

[19] W. K. Liu, S. Jun, and Y. F. Zhang, Reproducing kernel particle methods, International Journal for Numerical Methods in Fluids **20**, 1081 (1995).

[20] G. M. Zhang and R. C. Batra, Modified smoothed particle hydrodynamics method and its application to transient problems, Computational Mechanics **34**, 137 (2004).

[21] M. Liu, W. Xie, and G. Liu, Modeling incompressible flows using a finite particle method, Applied Mathematical Modelling **29**, 1252 (2005).

[22] D. Asprone, F. Auricchio, G. Manfredi, A. Prota, A. Reali, and G. Sangalli, Particle methods for a 1D elastic model problem: Error analysis and development of a second-order accurate formulation, Computer Modeling in Engineering & Sciences **62**, 1 (2010).

[23] D. Asprone, F. Auricchio, and A. Reali, Novel finite particle formulations based on projection methodologies, International Journal for Numerical Methods in Fluids **65**, 1376 (2011).

[24] S. J. Lind, B. D. Rogers, and P. K. Stansby, Review of smoothed particle hydrodynamics: towards converged Lagrangian flow modelling, Proceedings of the Royal Society A: Mathematical, Physical and Engineering Sciences **476**, 20190801 (2020).

[25] R. Feng, G. Fourtakas, B. D. Rogers, and D. Lombardi, Large deformation analysis of granular materials with stabilized and noise-free stress treatment in smoothed particle hydrodynamics (SPH), Computers and Geotechnics **138**, 104356 (2021).

[26] J. M. Domínguez, A. J. Crespo, M. Hall, C. Altomare, M. Wu, V. Stratigaki, P. Troch, L. Cappietti, and M. Gomez-Gesteira, SPH simulation of floating structures with moorings, Coastal Engineering **153**, 103560 (2019).

[27] J. R. King, S. J. Lind, B. D. Rogers, P. K. Stansby, and R. Vacondio, Large eddy simulations of bubbly flows and breaking waves with smoothed particle hydrodynamics, Journal of Fluid Mechanics **972**, A24 (2023).

[28] A. Khayyer, Y. Shimizu, C. H. Lee, A. Gil, H. Gotoh, and J. Bonet, An improved updated Lagrangian SPH method for structural modelling, Computational Particle Mechanics **11**, 1055 (2024).

[29] R. Feng, G. Fourtakas, B. D. Rogers, and D. Lombardi, A general smoothed particle hydrodynamics (SPH) formulation for coupled liquid flow and solid deformation in porous media, Computer Methods in Applied Mechanics and Engineering **419**, 116581 (2024).

[30] M. Schaller, J. Borrow, P. W. Draper, M. Ivkovic, S. McAlpine, B. Vandenbroucke, Y. Bahé, E. Chaikin, A. B. Chalk, T. K. Chan, *et al.*, Swift: a modern highly parallel gravity and smoothed particle hydrodynamics solver for astrophysical and cosmological applications, Monthly Notices of the Royal Astronomical Society **530**, 2378 (2024).

[31] S. J. Lind and P. Stansby, High-order Eulerian incompressible smoothed particle hydrodynamics with transition to Lagrangian free-surface motion, Journal of Computational Physics **326**, 290 (2016).

[32] A. M. Nasar, G. Fourtakas, S. J. Lind, J. King, B. D. Rogers, and P. K. Stansby, High-order consistent SPH with the pressure projection method in 2-d and 3-d, Journal of Computational Physics **444**, 110563 (2021).

[33] J. P. Vila, On particle weighted methods and smooth particle hydrodynamics, Mathematical models and methods in applied sciences **9**, 161 (1999).

[34] A. N. Parshikov and S. A. Medin, Smoothed particle hydrodynamics using interparticle contact algorithms, Journal of computational physics **180**, 358 (2002).

[35] Z.-F. Meng, P.-N. Sun, Y. Xu, P.-P. Wang, and A.-M. Zhang, High-order Eulerian SPH scheme through W/TENO reconstruction based on primitive variables for simulating incompressible flows, Computer Methods in Applied Mechanics and Engineering **427**, 117065 (2024).

[36] M. Lin, G. Fourtakas, and B. D. Rogers, A novel high-order spectral incompressible smoothed particle hydrodynamics (ISPH) scheme with an immersed boundary method (IBM), Journal of Computational Physics , 114264 (2025).

[37] J. King, S. J. Lind, and A. M. Nasar, High order difference schemes using the local anisotropic basis function method, Journal of Computational Physics **415**, 109549 (2020).

[38] J. King and S. J. Lind, High-order simulations of isothermal flows using the local anisotropic basis function method (LABFM), Journal of Computational Physics **449**, 110760 (2022).

[39] S. Popinet, A quadtree-adaptive multigrid solver for the serre–green–naghdi equations, Journal of Computational Physics **302**, 336 (2015).

[40] W. Zhang, A. Almgren, V. Beckner, J. Bell, J. Blaschke, C. Chan, M. Day, B. Friesen, K. Gott, D. Graves, *et al.*, Amrex: a framework for block-structured adaptive mesh refinement, The Journal of Open Source Software **4**, 1370 (2019).

[41] R. Cant, U. Ahmed, J. Fang, N. Chakarborty, G. Nivarti, C. Moulinec, and D. Emerson, An unstructured adaptive mesh refinement approach for computational fluid dynamics of reacting flows, Journal of Computational Physics **468**, 111480 (2022).

[42] M. M. Proot and M. I. Gerritsma, A least-squares spectral element formulation for the Stokes problem, Journal of Scientific Computing **17**, 285 (2002).

[43] M. Zayernouri and G. E. Karniadakis, Exponentially accurate spectral and spectral element methods for fractional ODEs, Journal of Computational Physics **257**, 460 (2014).

[44] F. Naddei, M. de la Llave Plata, V. Couaillier, and F. Coquel, A comparison of refinement indicators for p-adaptive simulations of steady and unsteady flows using discontinuous Galerkin methods, Journal of Computational Physics **376**, 508 (2019).

[45] P. Mossier, A. Beck, and C.-D. Munz, A p-adaptive discontinuous Galerkin method with hp-shock capturing, Journal of Scientific Computing **91**, 4 (2022).

[46] W. F. Mitchell and M. A. McClain, A survey of hp-adaptive strategies for elliptic partial differential equations, in *Recent advances in computational and applied mathematics* (Springer, 2011) pp. 227–258.

[47] F. Basile, J.-B. Chapelier, M. de la Llave Plata, R. Laraufie, and P. Frey, Unstructured h-and hp-adaptive strategies for discontinuous Galerkin methods based on a posteriori error estimation for compressible flows, Computers & Fluids **233**, 105245 (2022).

[48] J. Slak and G. Kosec, Adaptive radial basis function–generated finite differences method for contact problems, International Journal for Numerical Methods in Engineering **119**, 661 (2019).

[49] H. Ji, F.-S. Lien, and E. Yee, A new adaptive mesh refinement data structure with an application to detonation, Journal of computational physics **229**, 8981 (2010).

[50] Y.-Y. Lian, K.-H. Hsu, Y.-L. Shao, Y.-M. Lee, Y.-W. Jeng, and J.-S. Wu, Parallel adaptive mesh-refining scheme on a three-dimensional unstructured tetrahedral mesh and its applications, Computer Physics Communications **175**, 721 (2006).

[51] J. Gou, X. Yuan, and X. Su, A high-order element based adaptive mesh refinement strategy for three-dimensional unstructured grid, International journal for numerical methods in fluids **85**, 538 (2017).

[52] J. Benito, F. Urena, L. Gavete, and R. Alvarez, An h-adaptive method in the generalized finite differences, Computer methods in applied mechanics and engineering **192**, 735 (2003).

[53] D. T. Oanh, O. Davydov, and H. X. Phu, Adaptive RBF-FD method for elliptic problems with point singularities in 2D, Applied Mathematics and Computation **313**, 474 (2017).

[54] W. Hu, N. Trask, X. Hu, and W. Pan, A spatially adaptive high-order meshless method for fluid–structure interactions, Computer Methods in Applied Mechanics and Engineering **355**, 67 (2019).

[55] R. Vacondio, B. D. Rogers, P. K. Stansby, P. Mignosa, and J. Feldman, Variable resolution for SPH: a dynamic particle coalescing and splitting scheme, Computer Methods in Applied Mechanics and Engineering **256**, 132 (2013).

[56] M. Jančič and G. Kosec, Strong form mesh-free hp-adaptive solution of linear elasticity problem, Engineering with Computers **40**, 1027 (2024).

[57] J. R. King, A mesh-free framework for high-order direct numerical simulations of combustion in complex geometries, Computer Methods in Applied Mechanics and Engineering **421**, 116762 (2024).

[58] W. Dehnen and H. Aly, Improving convergence in smoothed particle hydrodynamics simulations without pairing instability, Monthly Notices of the Royal Astronomical Society **425**, 1068 (2012).

[59] J. Wackers, G. Deng, E. Guilmineau, A. Leroyer, P. Queutey, and M. Visonneau, Combined refinement criteria for anisotropic grid refinement in free-surface flow simulation, Computers & Fluids **92**, 209 (2014).

[60] J. Banks, J. Hittinger, J. Connors, and C. Woodward, Numerical error estimation for nonlinear hyperbolic PDEs via nonlinear error transport, Computer methods in applied mechanics and engineering **213**, 1 (2012).

[61] M. Ebrahimnejad, N. Fallah, and A. R. Khoei, Adaptive refinement in the meshless finite volume method for elasticity problems, Computers & Mathematics with Applications **69**, 1420 (2015).

[62] K. J. Fidkowski and D. L. Darmofal, Review of output-based error estimation and mesh adaptation in computational fluid dynamics, AIAA journal **49**, 673 (2011).

[63] G. Kuru, M. de la Llave Plata, V. Couaillier, R. Abgrall, and F. Coquel, An adaptive variational multiscale discontinuous Galerkin method for large eddy simulation, in *54th AIAA aerospace sciences meeting* (2016) p. 0584.

[64] P.-O. Persson and J. Peraire, Sub-cell shock capturing for discontinuous Galerkin methods, in *44th AIAA aerospace sciences meeting and exhibit* (2006) p. 112.

[65] J. D. Cole, On a quasi-linear parabolic equation occurring in aerodynamics, Quarterly of Applied Mathematics **9**, 225 (1951).

[66] E. S. Kordyban and T. Ranov, Mechanism of slug formation in horizontal two-phase flow, Journal of Basic Engineering **92**, 857 (1970).

[67] P. Lin and T. Hanratty, Prediction of the initiation of slugs with linear stability theory, International Journal of Multiphase Flow **12**, 79 (1986).

[68] D. J. Price, Modelling discontinuities and Kelvin–Helmholtz instabilities in SPH, Journal of Computational Physics **227**, 10040 (2008).

[69] M. J. Chen and L. K. Forbes, Accurate methods for computing inviscid and viscous Kelvin–Helmholtz instability, Journal of Computational Physics **230**, 1499 (2011).

[70] M. S. Shadloo and M. Yildiz, Numerical modeling of Kelvin–Helmholtz instability using smoothed particle hydrodynamics, International Journal for numerical methods in engineering **87**, 988 (2011).

[71] S. Gordon and B. J. McBride, *Computer Program for Calculation of Complex Chemical Equilibrium Compositions, Rocket Performance, Incident and Reflected Shocks, and Chapman-Jouguet Detonations. Interim Revision*, Tech. Rep. (1976).

[72] J. Li, Z. Zhao, A. Kazakov, and F. L. Dryer, An updated comprehensive kinetic model of hydrogen combustion, International journal of chemical kinetics **36**, 566 (2004).

[73] A. Domínguez-González, D. Martínez-Ruiz, and M. Sánchez-Sanz, Stable circular and double-cell lean hydrogen-air premixed flames in quasi two-dimensional channels, Proceedings of the Combustion Institute **39**, 1731 (2023).

[74] A. Ern and V. Giovangigli, *Multicomponent transport algorithms*, Vol. 24 (Springer Science & Business Media, 1994).

[75] A. Ern and V. Giovangigli, Fast and accurate multicomponent transport property evaluation, Journal of Computational Physics **120**, 105 (1995).

[76] J. O. Hirschfelder, C. F. Curtiss, and R. B. Bird, *The molecular theory of gases and liquids* (John Wiley & Sons, 1964).

[77] T. Howarth and A. Aspden, An empirical characteristic scaling model for freely-propagating lean premixed hydrogen flames, Combustion and Flame **237**, 111805 (2022).

[78] J. R. C. King, The Scalable Unstructured NodeSET code, `https://github.com/sunset_codes` (2024).

[79] R. S. Cant, *SENGA2 User Guide*, Tech. Rep. CUED/A-THERMO/TR67 (Cambridge University Engineering Department, 2012).

[80] R. S. Cant, U. Ahmed, J. Fang, N. Chakarborty, G. Nivarti, C. Moulinec, and D. R. Emerson, An unstructured adaptive mesh refinement approach for computational fluid dynamics of reacting flows, Journal of Computational Physics **468**, 111480 (2022).